Holographic laser Doppler ophthalmoscopy

M. Simonutti,[1,2] M. Paques,[1,2] J. A. Sahel,[1,2] M. Gross,[3] B. Samson,[4] C. Magnain,[4] and M. Atlan[4,*]

[1]*Institut de la Vision, Institut National de la Santé et de la Recherche Médicale (INSERM)–101, UMR-S 968, rue de Tolbiac, 75654 Paris Cedex 13, France*

[2]*Centre National de la Recherche Scientifique (CNRS) UMR 7210, Université Pierre et Marie Curie (UPMC) 75012 Paris, France*

[3]*Laboratoire Kastler-Brossel de l'École Normale Supérieure, CNRS UMR 8552, UPMC, 24 rue Lhomond 75005 Paris, France*

[4]*Institut Langevin, CNRS UMR 7587, INSERM U 979, Fondation Pierre-Gilles de Gennes, UPMC, Université Paris 7, ESPCI ParisTech, 10 rue Vauquelin, 75005 Paris, France*
*Corresponding author: atlan@optique.espci.fr

We report laser Doppler ophthalmoscopic fundus imaging in the rat eye with near-IR heterodyne holography. Sequential sampling of the beat of the reflected radiation against a frequency-shifted optical local oscillator is made onto an array detector. Wide-field maps of fluctuation spectra in the 10 Hz to 25 kHz band exhibit angiographic contrasts in the retinal vascular tree without requirement of an exogenous marker. © 2010 Optical Society of America

OCIS codes: 170.4470, 170.0110, 170.3340.

Retinal blood flow plays a pivotal role in several blinding diseases, such as diabetic retinopathy and vascular occlusions. While currently available optical instrumentation is well adapted for imaging retinal vessels, there are still technological limitations of currently available methods for retinal blood flow measurement that impair their clinical applications. Self-beating intensity fluctuations from a laser spot focused in the eye fundus was demonstrated to enable retinal flow assessment [1–3] noninvasively. It paved the way for the development of spatial scanning techniques, such as confocal spot [4] or line [5] scanning Doppler ophthalmoscopy. Yet laser Doppler methods for retinal blood flow mapping are still limited in term of velocity resolution and mapping capabilities.

Optical coherence tomography, commonly used for structural retinal layers imaging, was translated to a depth-resolved functional Doppler-contrast technique [6,7]. Optical microangiography further improved depth-resolved Doppler measurements for eye fundus imaging [8]. Such techniques can enable quantitative and directional flow assessment, but vessel segmentation is required [9,10].

Our approach to functional Doppler imaging is based on the detection of light fluctuations with an array detector. Multiply scattered light yields Doppler spectra from which the directional information of flow is lost because of wave-vector randomization. Nevertheless, it provides a spatially resolved hemodynamic contrast in low-light illumination conditions. In this Letter, we demonstrate experimentally the feasibility of wide-field holographic laser Doppler ophthalmoscopy *in vivo*.

The experimental ophthalmoscope realized for this study is based on the heterodyne imaging scheme described in [11]. It consists of a Mach–Zehnder laser interferometer in an off-axis and frequency-shifting configuration. The detection scheme is sketched in Fig. 1. A laser diode provides the main near-IR radiation at wavelength $\lambda = 785$ nm, polarized linearly. In the object arm, a polarizing beam splitter cube is used to illuminate the preparation and collect the cross-polarized backscattered light component, in order to increase the relative weight of multiply scattered Doppler-shifted photons with respect to

photons scattered once [12]. Three adult rats were used for the preparations. Anesthesia was induced by intraperitoneal injection of 100 mg/kg ketamine and 25 mg/kg xylazine (both from Sigma-Aldrich). Topical tropicamide (CibaVision) was administered for pupil dilation. Each rat was placed on its side under the illumination beam. The head was supported so that the iris was perpendicular to the illumination axis. After administration of topical oxybuprocaine (CibaVision), a coverslip was applied on a ring surrounding the globe. Methylcellulose (Goniosol) was applied as a contact medium. The incident optical field E_I is expanded to form a plane wave. Illumination power within 5 mm × 5 mm at the object plane is ∼1 mW. In the reference arm [(local oscillator (LO)], an attenuator, a half-wave plate, and a beam expander (not shown) are used to control the beam power, polarization angle, and to ensure a roughly flat LO illumination of the detector. The optical frequency detuning $\Delta\omega$ between the two optical channels is imposed by acousto-optic modulators. The backscattered field E is combined with the LO field E_{LO} with a nonpolarizing beam splitter cube. The detuning $\Delta\omega$ shifts a component of interest of the scattered field temporal fluctuation spectrum within the actual camera bandwidth (temporal heterodyning). Moreover, a small angular tilt θ_0, ϕ_0 of ∼1°, ensures off-axis mixing
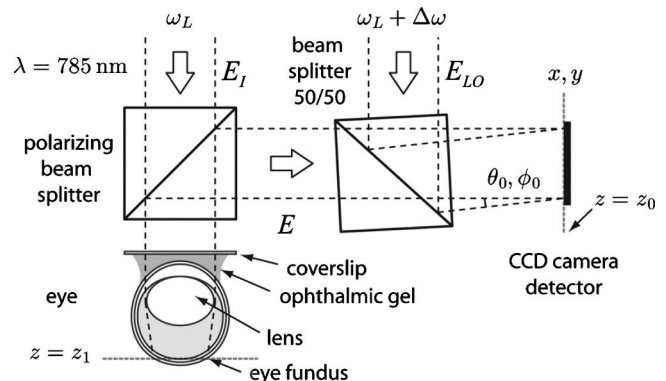

Fig. 1. Optical configuration. The eye fundus is illuminated in broad field through the dilated iris. The cornea curvature is compensated by a coverslip and ophthalmic aqueous gel.

© 2010 Optical Society of America

conditions that shift the spatial frequency spectrum of the recorded object field (spatial heterodyning). The interference pattern $I = |E + E_{LO}|^2$ is measured by a Sony ICX 285AL CCD array sensor (gain, $3.8e/\text{count}$), from which the central 1024×1024 pixel region is read out at 10 Hz. The detector is set $\sim$30 cm away from the object plane. The recorded intensity pattern I_n at time t_n in the detector plane ($z = z_0$) is

$$I_n = |\mathcal{E}|^2 + |\mathcal{E}_{LO}|^2 + \mathcal{E}\mathcal{E}_{LO}^* e^{-i(\Delta\omega t_n + \Delta k_x x + \Delta k_y y)}$$
$$+ \mathcal{E}^* \mathcal{E}_{LO} e^{+i(\Delta\omega t_n + \Delta k_x x + \Delta k_y y)}, \qquad (1)$$

where $\mathcal{E}$ and $\mathcal{E}_{LO}$ are the complex envelopes of the scattered and LO fields, respectively. $\Delta k_x = 2\pi \sin(\theta_0)/\lambda$ and $\Delta k_y = 2\pi \sin(\phi_0)/\lambda$ are the projections of the difference between the LO and the signal wave vectors in the transverse (x, y) plane. $*$ denotes the complex conjugate. The two first terms of the right-hand side of Eq. (1) are the self-beating (homodyne) contributions of E and E_{LO}. The heterodyne signal of interest lies in the third term. The fourth term is the twin-image (ghost) contribution.
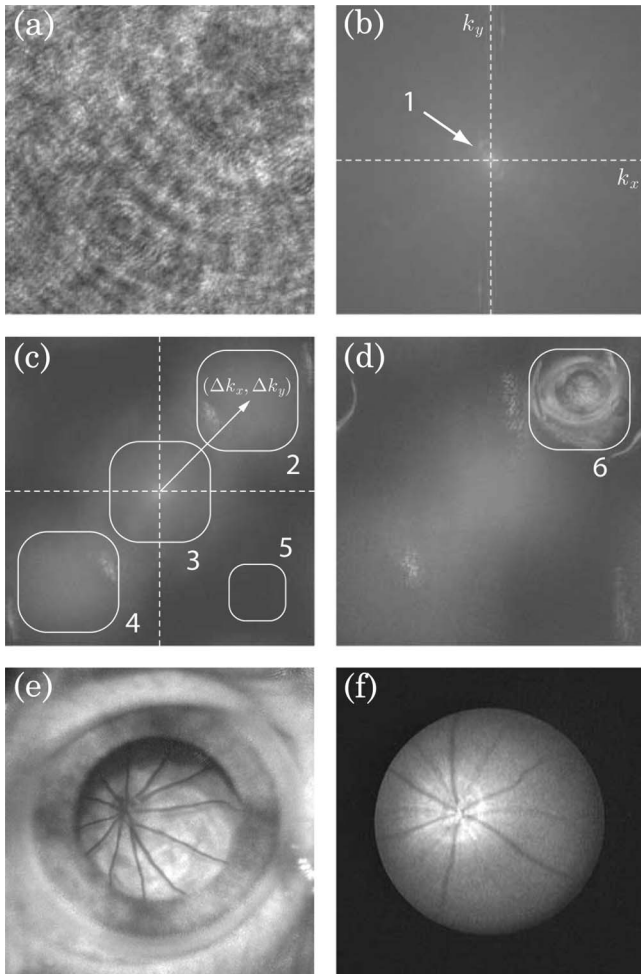

Fig. 2. (a) Recorded interference pattern, $\Delta\omega/(2\pi) = 10$ Hz. (b) FFT of the recorded frame. The dominating noise (1) is gathered in the low spatial frequencies. (c) FFT of the difference of two consecutive frames. Heterodyne contributions (2,4), homodyne contributions (3), noise (5). (d) Image focus (6) by Fresnel transform. (e) Magnified view of the retina. (f) White-light endoscopic view of the retina.

A typical interference pattern I_n of E beating against E_{LO} is shown in Fig. 2(a). The magnitude of the fast spatial Fourier transform (FFT) of one recorded frame $|\text{FFT}(I_n)|^2$ mainly carries the LO contribution in the high heterodyne gain regime, when the optical power in the LO channel is larger than in the object channel [Fig. 2(b)]. Since the LO beam exhibits flat-field fluctuations, its self-beating contribution is gathered in the low-frequency region 1 in reciprocal space (k_x, k_y). Making the difference of two consecutive frames before (or after) applying the spatial Fourier transform yields $|\text{FFT}(I_{n+1} - I_n)|^2$; it decreases substantially the relative weight of the LO self-beating term, showing up the object-against-LO beating term and the ghost term [regions 2 and 4, respectively, in Fig. 2(c)]. The object beam self-beating term also appears, in region 3. Detection noise is assessed in region 5. Because of off-axis geometry, the heterodyne signal contribution is shifted away, by $\pm(\Delta k_x, \Delta k_y)$, from self-beating field contributions. In on-axis geometry ($\Delta k_x = 0$, $\Delta k_y = 0$), all interferometric terms would overlap spatially. The object field can hence be assessed with much better sensitivity than if measured in either on-axis-only or off-axis-only conditions and used for numerical reconstruction of the signal S with a discrete Fresnel transform:

$$S = |\text{FFT}((I_{n+1} - I_n)e^{i\frac{\pi}{\lambda\Delta z}(x^2 + y^2)})|^2,$$

where the distance parameter used for free-space back-propagation of the optical field is $\Delta z = z_1 - z_0 = 26.6$ cm. Once accurate focus is found, the fundus image appears as reported in Fig. 2(d), in region 6, magnified in Fig. 2(e). These Doppler images are time-averaged $\langle S \rangle$; angular brackets $\langle \rangle$ account for averaging over 32 frames. The star-shaped vascular tree of the rat eye fundus is clearly visible and consistent with the white-light
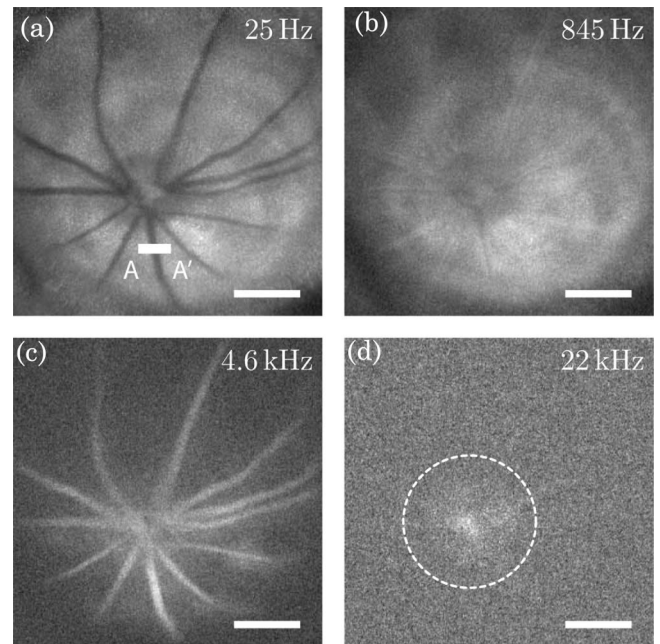

Fig. 3. Doppler fundus images at four frequency detunings $\Delta\omega/(2\pi)$. Optical power is displayed in logarithmic scale (white is for high signal). $[AA']$ indicates the measurement region of the lines reported in Fig. 4(a). Scale bar, 1 mm.

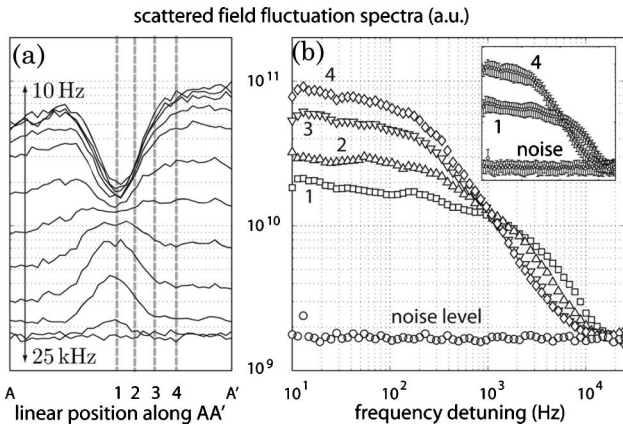scattered field fluctuation spectra (a.u.)

Fig. 4.   (a) $\langle S \rangle$ against position along $[AA']$ of Fig. 3(a), averaged over 15 pixels in the orthogonal direction. Traces correspond to logarithmically spaced detuning frequencies from 10 Hz to 25 kHz. (b) $\langle S \rangle$ against $\Delta\omega$ at positions 1, 2, 3, and 4 from the center of the vessel to its periphery.

endoscopic image performed afterward in the same preparation, displayed in Fig. 2(f).

Detuning $\Delta\omega$ slows down selectively the drift rate of the set of fringes associated to a given Doppler component, and sets it within the actual camera bandwidth. Frequency-selective eye fundus images $\langle S \rangle$ of a healthy rat at four LO detunings (25 Hz, 845 Hz, 4.6 kHz, and 22 kHz) are reported in Fig. 3. A contrast reversal is observed between vessels and surrounding retinal tissue (and, most likely, in the choroid) from low- to high-frequency detunings [Figs. 3(a) and 3(c)]. Fluctuation spectra lines $\langle S \rangle$ throughout a vessel cross section are reported in Fig. 4, as a function of position [Fig. 4(a)], and as a function of $\Delta\omega$, at four locations within the vessel [Fig. 4(b)]; typical spatial standard deviations of $\langle S \rangle$ are shown in the inset. It can be estimated that choroidal flow significantly contributed to the signal along the retinal vessel section $[AA']$. Within this vessel, the Doppler spectrum is clearly broader than those of immediate surrounding areas, showing that the retinal flow predominantly contributed to the signal in this specific zone. The broadest Doppler signal, which is still visible at 22 kHz in Fig. 3(d), is found in the optic nerve head region (circled); it is interpreted as a consequence of vessel orientation and increased density in this area.

In conclusion, we have demonstrated the feasibility of holographic laser Doppler ophthalmoscopy with near-infrared radiation. The illumination power over the whole eye fundus can be kept low ($\sim$1 mW). High detection sensitivity, in a moderate-to-high heterodyne gain regime, is achieved by spatiotemporal heterodyning, which enables an efficient rejection of parasitic interferometric contributions. Fluctuation spectra discrepancies below 25 kHz between the superficially vascularized regions and the surrounding retinal tissue layers provide an optical contrast suitable for angiographic mapping. A high reproducibility of the signal acquired over several hours, over repeated trials, and among different animals is observed. Potential applications are essentially the investigation of retinal and possibly choroidal vascular diseases. At the current stage, there are yet limitations due to suboptimal lateral, depth, and time resolution, which, for instance, do not allow detection of heart-beat-related flow variations. Technical improvements are expected to circumvent these problems.

References

1. C. E. Riva, G. T. Feke, B. Eberli, and V. Benary, Appl. Opt. **18**, 2301 (1979).
2. Y. Aizu, K. Ogino, T. Sugita, T. Yamamoto, N. Takai, and T. Asakura, Appl. Opt. **31**, 3020 (1992).
3. H. Fujii, Med. Biol. Eng. Comput. **32** (302), 1994.
4. G. Michelson, B. Schmauss, M. J. Langhans, J. Harazny, and M. J. Groh, J. Glaucoma **5**, 99 (1996).
5. R. D. Ferguson, D. X. Hammer, A. E. Elsner, R. H. Webb, S. A. Burns, and J. J. Weiter, Opt. Express **12** 5198 (2004).
6. Z. Chen, T. E. Milner, S. Srinivas, X. Wang, A. Malakzali, M. J. C. van Gemert, and J. S. Nelson, Opt. Lett. **22**, 1119 (1997).
7. J. A. Izatt, M. D. Kulkarni, S. Yazdanfar, J. K. Barton, and A. J. Welch, Opt. Lett. **22**, 1439 (1997).
8. L. An and R. K. Wang, Opt. Express **16**, 11438 (2008).
9. Y. Wang, B. A. Bower, J. A. Izatt, O. Tan, and D. Huang, J Biomed. Opt. **12**, 041215 (2007).
10. R. Michaely, A. H. Bachmann, M. L. Villiger, C. Blatter, T. Lasser, and R. A. Leitgeb, J. Biomed. Opt. **12**, 041213 (2007).
11. M. Atlan, M. Gross, T. Vitalis, A. Rancillac, B. C. Forget, and A. K. Dunn, Opt. Lett. **31**, 2762 (2006).
12. J. M. Schmitt, A. H. Gandjbakhche, and R. F. Bonner, Appl. Opt. **31**, 6535 (1992).